Giant, 6, 2021, 100055

Full-length article

Effect of crystallization of the polyhedral oligomeric silsesquioxane block on self-assembly in hybrid organic-inorganic block copolymers with salt

Gurmukh K. Sethi[a,b,1], **Saheli Chakraborty**[e,1], **Chenhui Zhu**[f], **Eric Schaible**[f], **Irune Villaluenga**[g,h,2], **Nitash P. Balsara**[b,c,d,e,2]

[a] Department of Materials Science and Engineering University of California, Berkeley, CA 94720, USA
[b] Department of Chemical and Biomolecular Engineering, University of California, Berkeley, California 94720, USA
[c] Materials Science Division, Berkeley, California 94720, USA
[d] Joint Center for Energy Storage Research (JCESR), Berkeley, California 94720, USA
[e] Energy Storage and Distributed Resources Division, Berkeley, California 94720, USA
[f] Advanced Light Source, Lawrence Berkeley National Laboratory, Berkeley, California 94720, USA
[g] POLYMAT University of the Basque Country UPV/EHU, 20018 Donostia-San Sebastián, Spain
[h] Ikerbasque, Basque Foundation for Science, 48013 Bilbao, Spain

Keywords: Block copolymers, Hybrid, Electrolytes, Phase behavior, Phase separation, Phase transition, Self-assembly, Crystallization, Semi-crystalline polymers, POSS, Poly(ethylene oxide)

We present a DSC and X-ray scattering study investigating the effect of polyhedral oligomeric silsesquioxane (POSS) block crystallinity on the self-assembly of a poly(acryloisobutyl polyhedral oligomeric silsesquioxane)-*b*-poly(ethylene oxide)-*b*-poly(acryloisobutyl polyhedral oligomeric silsesquioxane) (POSS-PEO-POSS) triblock copolymer and poly(ethylene oxide)-*b*- poly(acryloisobutyl polyhedral oligomeric silsesquioxane) (PEO-POSS) diblock copolymers mixed with lithium bis(trifluoromethanesulfonyl)imide salt. The POSS block in all copolymer/salt mixture organizes into a rhombohedral crystal, similar to that of the POSS homopolymer. Semicrystalline polymer/salt mixtures favor morphologies with flat interfaces (*i.e.*, lamellae) despite the asymmetric nature of the copolymers; PEO/salt volume fractions range from 0 to 0.85. Coexisting lamellae and hexagonally packed cylinders as well as coexisting lamellae with different domain spacings are seen in many copolymer/salt mixtures wherein the POSS block is amorphous. Morphological phase transitions in these systems are seen in the vicinity of the POSS crystallization temperature.

1 Introduction

The self-assembly and phase behavior of block copolymers is a subject of continuing interest. It is generally believed that the morphology obtained in these systems is governed by four parameters: copolymer composition, chain length, molecular

E-mail addresses: iruneuskal@gmail.com (I. Villaluenga), nbalsara@berkeley.edu (N.P. Balsara).

Received 9 January 2021; Received in revised form 16 February 2021; Accepted 22 February 2021

[1] Equal contributions.
[2] Corresponding author.

 https://doi.org/10.1016/j.giant.2021.100055

List of Symbols

CYL	hexagonally packed cylinders morphology
d	domain spacing (nm)
d_{CYL}	domain spacing of hexagonally packed cylinders (nm)
d_{LAM}	domain spacing of lamellae (nm)
$d_{LAM,I}$	domain spacing of first lamellar phase (nm)
$d_{LAM,II}$	domain spacing of second lamellar phase (nm)
DIS	disordered morphology
f_{CYL}	fraction of hexagonally packed cylinders grains
f_{EO}	volume fraction of PEO microphase
$f_{EO/LiTFSI}$	volume fraction of PEO/LiTFSI microphase
I	X-ray scattering intensity
LAM	lamellar morphology
LAM/CYL	coexisting lamellar/hexagonally packed cylinders morphology
LAM/LAM	coexisting lamellar/lamellar morphology
L_{cry}	crystallite size (nm)
M_{EO}	molecular weight of the poly(ethylene oxide) unit (kg mol^{-1})
M_i	molecular weight of species i (g mol^{-1})
M_P	molecular weight of the polyhedral oligomeric silsesquioxane unit (kg mol^{-1})
M_{PEO}	molecular weight of the poly(ethylene oxide) block (kg mol^{-1})
M_{POSS}	molecular weight of the polyhedral oligomeric silsesquioxane block (kg mol^{-1})
N	degree of polymerization
N_i	degree of polymerization of species i
q	scattering vector (nm^{-1})
q^*	scattering vector at the primary scattering peak (nm^{-1})
$q_1{}^*$	scattering vector at the first primary scattering peak (nm^{-1})
$q_2{}^*$	scattering vector at the second primary scattering peak (nm^{-1})
r	salt concentration ([Li] [EO]$^{-1}$)
$S_{\sqrt{3}q*}$	SAXS invariant centered around $q = \sqrt{3}q*$
S_{2q*}	SAXS invariant centered around $2q^*$
S_T	SAXS invariant at $q = q^*$ of the SAXS profile calculated at temperature, T
S_{Tmax}	SAXS invariant at the maximum temperature
T	temperature (°C)
T_c	POSS block crystallization temperature (°C)
T_m	POSS block melting temperature (°C)
w_{POSS}	weight fraction of POSS block
X_c	relative percent crystallinity of POSS block
x	molecular weight of PEO chain (kg mol^{-1})
y	molecular weight of the POSS chain (kg mol^{-1})

Greek

ΔH_m	Enthalpy of melting of the POSS block (J g^{-1})
θ	X-ray scattering angle
λ	X-ray wavelength (1.2398 Å)
v_{EO}	molar volume of ethylene oxide monomer unit (nm^3)
v_i	molar volume of unit i (nm^3)
v_{POSS}	molar volume of POSS monomer unit (nm^3)
v_{ref}	reference volume (0.1 nm^3)
ρ_i	density of unit i (g cm^{-3})
ρ_{PEO}	density of PEO chain (g cm^{-3})
ρ_{POSS}	density of POSS chain (g cm^{-3})

architecture (diblock versus triblock copolymer), and Flory Huggins interaction parameter, χ. Microphase separation is observed when χN exceeds a critical value [1]. This is, however, only true for systems wherein both blocks are amorphous; most of the systematic experimental and theoretical studies in this field have focused on this case [2–6]. In a pioneering study, Whitmore and Noolandi predicted the phase behavior of systems wherein one of the blocks was semicrystalline, assuming that only lamellar morphologies would be obtained [7]. This assumption is reasonable as semicrystalline polymer chains fold into lamellar motifs which are commensurate with the self-assembled lamellar morphology [8–10]. It is important to distinguish between lamellae formed by folded crystalline polymers which are obtained in both homopolymer and block copolymers and lamellae formed by block copolymers due to microphase separation. However, relatively few studies have been conducted on such systems [11–13]. Compared to amorphous systems, our knowledge of the factors that control the morphology of semicrystalline block copolymers is limited. For instance, it is not clear if a semicrystalline block copolymer can be disordered (*i.e.* one of the blocks forms crystals but the block copolymer does not exhibit microphase separation).

There is a growing interest in the morphology of block copolymers with added salt due to their potential applications as solid electrolytes in rechargeable batteries [14]. The ions are segregated in the amorphous block, usually poly(ethylene oxide) above the crystalline melting temperature. The mechanical properties of these electrolytes are controlled mainly by the nonconducting block. While in principle the nonconducting block could be either glassy or semicrystalline, most studies to date have focused on glassy blocks such as poly(styrene) [15,16].

In this paper, we study the effect of added salt on morphology in three hybrid organic-inorganic block copolymers: two poly(ethylene oxide)-*b*-poly(acryloisobutyl polyhedral oligomeric silsesquioxane) (PEO−POSS(x-y)) diblock copolymers and a poly(acryloisobutyl polyhedral oligomeric silsesquioxane)-*b*-poly(ethylene oxide)-*b*-poly(acryloisobutyl polyhedral oligomeric silsesquioxane) (POSS-PEO-POSS(y-x-y)) triblock copolymer (x and y refer to the molecular weight of the PEO block and the POSS block in kg mol^{-1} rounded to the nearest whole number). The chemical structures of PEO-POSS and POSS-PEO-POSS are shown in Scheme 1a and b. The first diblock copolymer, PEO-POSS(5–2), contains PEO and POSS blocks with molecular weights of 5 and 1.9 kg mol^{-1}, respectively. The second diblock copolymer, PEO-POSS(10–4) is similar but has double the molecular weight (PEO and POSS blocks with molecular weights of 10 and 3.8 kg

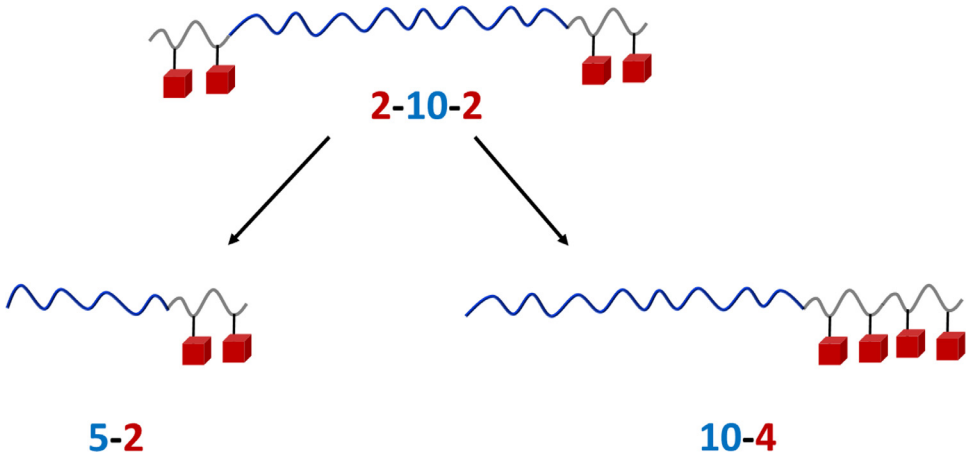

Fig. 1

Hybrid organic-inorganic copolymer chemical structure cartoons. Triblock copolymer, POSS-PEO-POSS(2–10–2) is cut in half to make the smaller diblock copolymer, PEO-POSS(5–2), and is rearranged to form the larger diblock copolymer, PEO-POSS(10–4).

mol $^{-1}$, respectively). The triblock copolymer, POSS-PEO-POSS(2–10–2), contains a PEO chain flanked by POSS segments, and the molecular weights of the PEO and POSS blocks are 10 and 1.9 kg mol $^{-1}$, respectively. The volume fraction of the PEO block, f_{EO}, is 0.76 in all three block copolymers. The salt used in this study is lithium bis(trifluoromethanesulfonyl)imide (LiTFSI). It has been noted that the self-assembly of triblock copolymers is similar to that of diblock copolymers obtained by cutting the chains in the middle [17–21]. PEO-POSS(5–2) and POSS-PEO-POSS(2–10–2) allow for the study of this effect. Comparing PEO-POSS(10–4) and POSS-PEO-POSS(2–10–2) enables a study of the effect of molecular architecture (diblock versus triblock copolymers) at fixed volume fraction and chain length. The three polymers are shown in Fig. 1.

This paper is a part of a series studying the morphology and thermodynamic properties of PEO and POSS-containing copolymers. In ref [22], we discuss the reversible order-to-disorder transition upon heating in a PEO-POSS(5–1)/salt mixture using SAXS and NMR. In ref [23], we analyzed the phase behavior of a series of PEO-POSS(5–2)/salt mixtures as a function of temperature and salt concentration. In ref [24], we determined the morphology of a series of PEO-POSS diblock copolymer/salt mixtures of varied molecular weight, volume fraction, salt concentration, and temperature. The morphology was interpreted using χ determined by analyzing the scattering from disordered systems. We missed the fact that the POSS block was semicrystalline in ref [22–24]. More recently, in ref [25], we discuss the effect of POSS-block crystallinity on the reversibility of grain structure changes upon heating and cooling in one POSS-PEO-POSS(2–10–2)/salt mixture.

In the present study, we begin with a detailed study of the semicrystalline nature of the POSS block using differential scanning calorimetry and wide-angle X-ray scattering. This is followed by determination of the morphology using small-angle X-ray scattering. We conclude by exposing the effect of crystallization on morphology.

2 Experimental

2.1 Materials

PEO-acrylate (M_{PEO} = 10 kg mol^{-1}), lithium bis(trifluoromethanesulfonyl)-imide, Li[N(SO_2CF_3)$_2$] (LiTFSI), tetrahydrofuran, toluene and 1,4-dioxane was purchased from Sigma-Aldrich. Acryloisobutyl POSS was purchased from Hybrid Plastics. BlocBuilder MA was kindly provided by Arkema. All chemicals were used as received.

2.2 Synthesis

PEO-POSS block copolymers were synthesized by nitroxide mediated radical polymerization (NMP). as described in ref [23]. POSS-PEO-POSS block copolymer was synthesized by atom transfer radical polymerization (ATRP) as described in ref [25]. POSS homopolymer synthesis is performed by combining 5 g acryloisobutyl POSS (5.4 mmol) with 103 mg (0.27 mmol) BlocBuilder MA and 50 mL 1,4-dioxane. The solution was purged with N_2 for 30 min. The reaction occurred at 90 °C for 5 h. The product was cooled, and pure polymer was obtained by reprecipitating 5 times in cold methanol. Molecular weight was determined using ^{1}H NMR spectroscopy. GPC traces the POSS homopolymer confirm the polymerization of the POSS block. Due to the complex molecular structure and potential interactions between the polymer segments and the columns, we only use the GPC data to confirm the POSS polymerization [23,25].

The polymers used in this study are called POSS-PEO-POSS(*x*-*y*-*x*) and PEO-POSS(*x*-*y*) where *x* and *y* are the molecular weights of the PEO, M_{PEO}, and POSS, M_{POSS}, blocks in kg mol^{-1} respectively. POSS-PEO-POSS and PEO-POSS structures are shown in Scheme 1. The overall degree of polymerization (N_i) of each block was calculated by

$$N_i = \frac{M_i}{\rho_i v_{ref}} \quad (1)$$

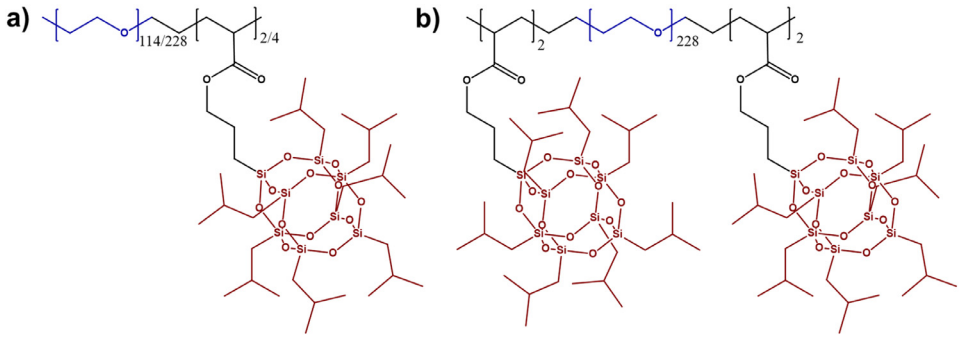

Scheme 1

Hybrid organic-inorganic copolymer chemical structures. a) PEO-POSS chemical structure where POSS repeat units are 2 in PEO-POSS(5–2) or 4 in PEO-POSS(10–4) and EO repeat units are 114 in PEO-POSS(5–2) and 228 in PEO-POSS(10–4). b) POSS-PEO-POSS(2–10–2) chemical structure where POSS repeat units are 2 at both the chain ends and EO repeat units are 228.

Table 1

Characteristics of polymers in this study.

Polymer	M_{PEO}(kg mol^{-1})	M_{POSS}(kg mol^{-1})	N(120 °C)	f_{EO}(120 °C)
POSS(4)	0	3.72	47	0
POSS-PEO-POSS(2–10–2)	10	3.72	194	0.76
PEO-POSS(5–2)	5	1.86	97	0.76
PEO-POSS(10–4)	10	3.72	194	0.76

M_{PEO} = molecular weight of the PEO block; M_{POSS} = molecular weight of the POSS block determined by H–NMR; N = chain length calculated at 120 °C and monomer reference volume of 0.1 nm^3; f_{EO} = volume fraction of PEO block at 120 °C.

where v_{ref} is fixed at 0.1 nm^3, as described in ref [26]. The overall degree of polymerization was calculated by

$$N = N_{PEO} + N_{POSS}. \tag{2}$$

M_P and M_{EO} are the molar mass of POSS (929.61 g mol^{-1}) and EO monomer units (44.05 g mol^{-1}) respectively; v_{EO} and v_{POSS} are the molar volumes of ethylene oxide monomer units and POSS monomer units calculated using the following equation

$$v_i = \frac{M_i}{\rho_i} \tag{3}$$

where M_i and ρ_i are the molar masses of unit i and density of unit i, respectively. ρ_{PEO} = 1.128 g cm^{-3} [27] and ρ_{POSS} = 1.30 g cm^{-3} at 120 °C. Volume fraction is calculated by

$$f_{EO} = \frac{v_{EO}}{v_{EO} + \frac{M_{POSS}M_{EO}}{M_P M_{PEO}} v_{POSS}} \tag{5}$$

Table 1 shows the polymer characteristics of the three polymers used in this study.

2.3 Electrolyte preparation

Polymer/salt mixtures were prepared by mixing each polymer with LiTFSI. All mixtures were prepared in an argon glovebox (MBraun) where H_2O and O_2 levels were maintained below 0.5 ppm. POSS-PEO-POSS and PEO-POSS polymers were dried at 90 °C in a glovebox antechamber under vacuum for 48 h. LiTFSI salt was dried at 120 °C for 72 h under active vacuum. Dry polymer and dry LiTFSI salt were then dissolved into THF and the solutions were well-mixed at 55 °C for 24 h. Once dissolved, THF was evaporated at 60 °C for 24 h. The homogenous polymer/salt mixtures were further dried on a hotplate at 90 °C for 48 h, then transferred to the glovebox antechamber and additionally dried under vacuum for 72 h at 90 °C to remove residual solvent. The dry electrolytes color ranged from clear to milky white to pale yellow at room temperature with a solid or waxy consistency. Salt concentrations are calculated by the ratio of lithium to ethylene oxide monomer units (r = [Li] [EO]$^{-1}$).

2.4 Differential scanning calorimetry

Samples were hermetically sealed using Tzero aluminum pans and lids in an argon glovebox. Differential scanning calorimetry (DSC) thermograms were obtained by 2 heating and cooling cycles with 20 °C min^{-1} heating rates and 2 °C min^{-1} cooling rates using a Thermal Advantage Q200 calorimeter at the Molecular Foundry, Lawrence Berkeley National Laboratory. The temperature ranged from −90 to 160 °C. Melting and glass transition temperatures were ascertained by analyzing the second heating scan and crystallization transition temperatures was ascertained by analyzing the first cooling scan using TA Thermal Advantage software.

2.5 Small and wide-angle X-ray scattering

The morphologies and crystallinity of the electrolytes were determined by small-angle X-ray scattering (SAXS) and wide-angle X-ray scattering (WAXS) respectively. Sample preparation took place inside an argon glovebox. Neat polymers and polymer/salt mixtures were heated to 120 °C, then pressed into 1 mm thick rubber spacers with a 1/8 in. inner-diameter to create a uniform film. The spacers were then sealed inside Kapton windows in custom airtight holders. The samples were annealed at 120 °C under vacuum for at least 48 h. Measurements were performed at beamline 7.3.3. at the Advanced Light Source (ALS) at Lawrence

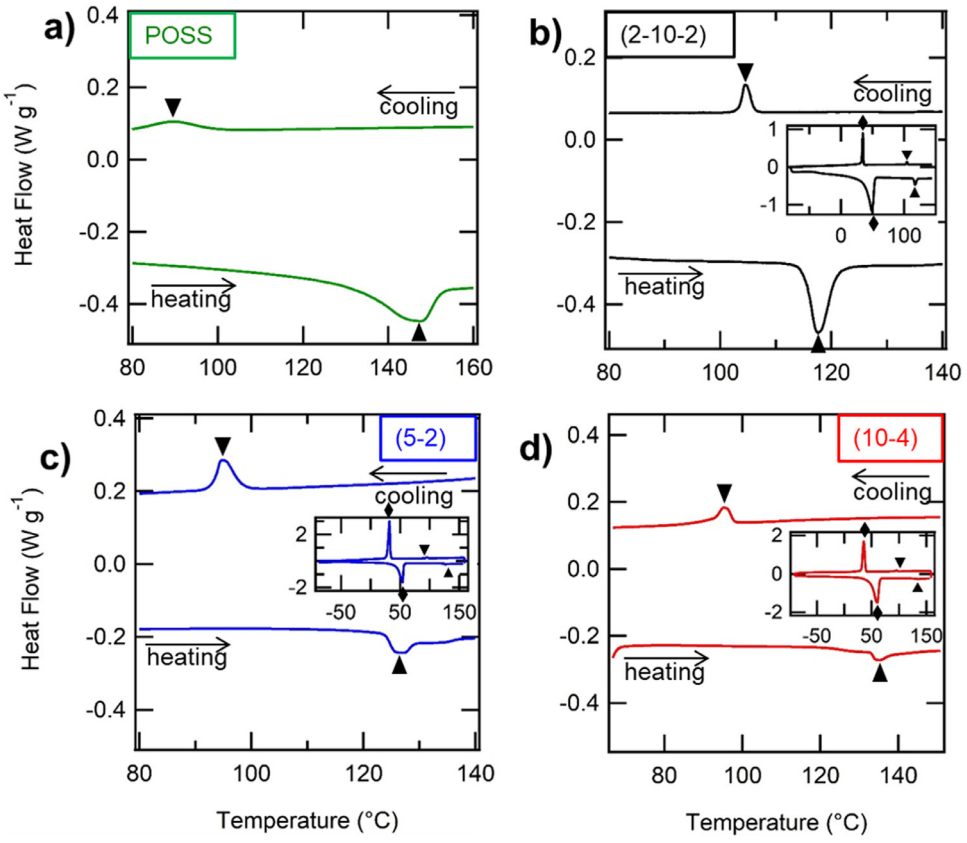

Fig. 2

DSC thermograms upon cooling and second heating in a) neat POSS homopolymer and copolymers with salt concentration $r = 0.02$ b) POSS-PEO-POSS(2–10–2) c) PEO-POSS(5–2), and d) PEO-POSS(10–4). Insets in b-d show thermograms at larger temperature range.

Berkeley National Laboratory and beamline 1–5 at the Stanford Synchrotron Radiation Lightsource (SSRL) at SLAC National Accelerator Laboratory. Using a custom-built heat stage, samples were heated in 20 °C to 60 °C increments, from room temperature up to a maximum of 145 °C, holding temperature at each step for at least 30 min, and then cooled in increments between 5 °C and 20 °C. At the end of each temperature step, SAXS/WAXS measurements were made to establish morphology and confirm thermo-reversibility of phase behavior. Silver behenate was used to determine the beam center and sample-to-detector distance. Two-dimensional scattering patterns were integrated azimuthally using the Nika program for IGOR Pro-to produce one-dimensional scattering profiles [28]. Here we report the scattering intensity as a function of the magnitude of the scattering vector, q ($q = 4\pi sin(\theta/2)/\lambda$) where θ is the scattering angle, and λ is the wavelength of the X-rays equal to 1.2398 Å at the ALS and 1.03232 Å at SSRL.

3 Results and discussion

3.1 Crystallization of the POSS block

DSC thermograms of the neat POSS homopolymer is shown in Fig. 2a. We observe a melting transition at temperature, $T_m = 144.4$ °C during the heating scan and a crystallization transition at temperature, $T_c = 89.5$ °C in the cooling scan. In Figs. 2b-d, we show typical DSC thermograms of copolymer/salt mixtures in the temperature range $80 \leq T \leq 140$ °C, focusing on the crystallization and melting of the POSS block. Because the POSS blocks are short, we do not expect chain folding of the POSS block in any of the block copolymers. The salt concentration of all three systems is [Li] $[EO]^{-1} = r = 0.02$. All three systems exhibit signatures of POSS melting and crystallization. The insets in Figs. 2b-d show the thermograms on a wider temperature scale where the closed diamonds reflect the melting and crystallization of PEO domains. In all copolymer/salt mixtures, the DSC peaks associated with the PEO melting and crystallization are much more pronounced than those associated with POSS melting and crystallization.

WAXS intensity, $I(q)$, is obtained from POSS homopolymer at selected temperatures, plotted as a function of the magnitude of the scattering vector, q in Fig. 3a. The sample was heated from room temperature from 25 to 141 °C. The sharp peaks at $q = 5.9$ nm^{-1}, 7.9 nm^{-1}, and 8.9 nm^{-1} observed at 25 °C and 85 °C indicate the presence of the crystalline phase. These peaks give way to an amorphous halo at 141 °C. This scattering pattern indicates the rhombohedral packing of the POSS macromonomer crystal [29–37]. The peak visible at $q = 4.0$ nm^{-1}, is due to the Kapton widows and is apparent in all of the WAXS scans. When the sample is cooled from 141 °C to 85 °C, the crystalline peaks are sharper than those obtained during the heating scan [34].

WAXS profiles of POSS-PEO-POSS(2–10–2) $r = 0.02$ (Fig. 3b) at 25 °C reveal three peaks similar to those found in the POSS

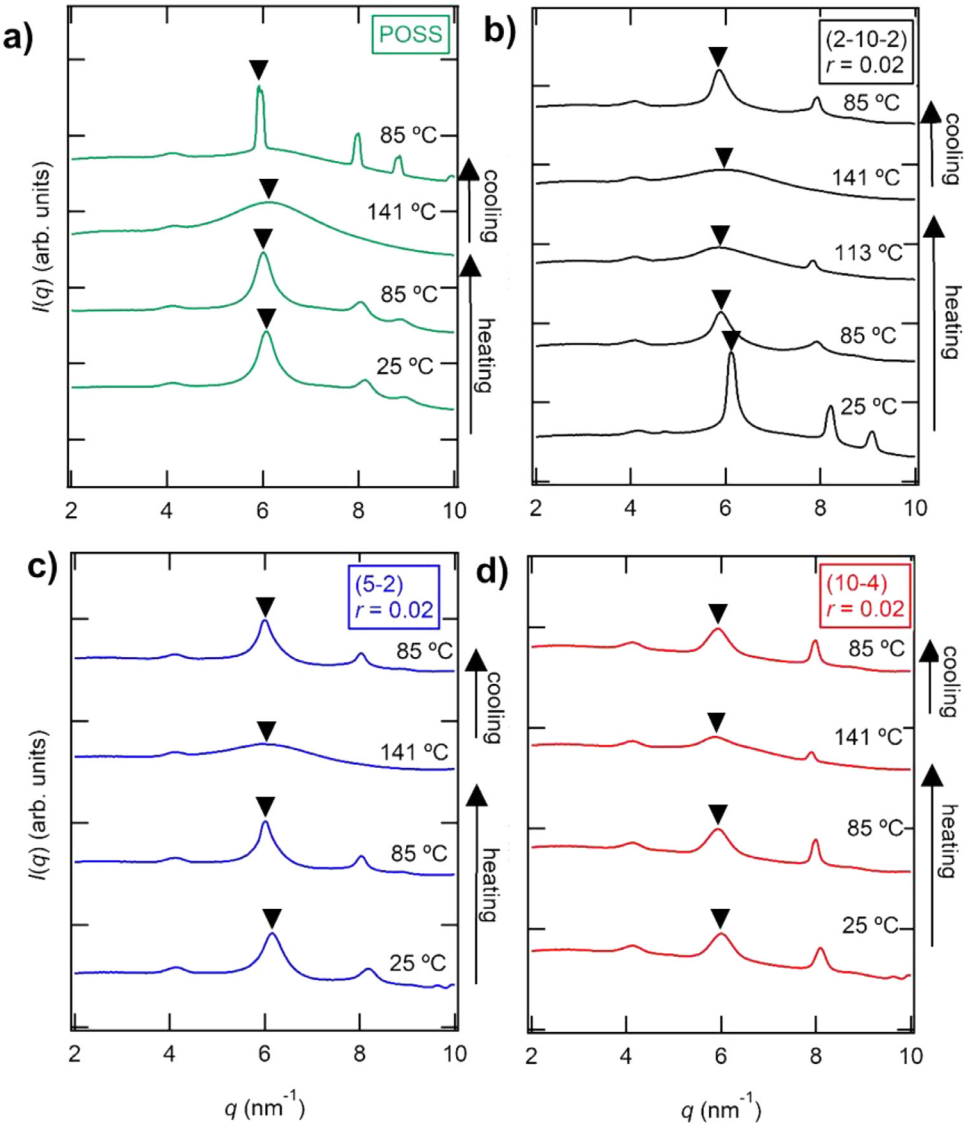

Fig. 3

WAXS intensity is plotted as a function of the magnitude of the scattering vector, q, in a) neat POSS homopolymer as well as copolymer/salt mixtures at $r = 0.02$, b) POSS-PEO-POSS(2–10–2), c) PEO-POSS(5–2), d) PEO-POSS(10–4). Profiles are shifted vertically. Scans are performed upon heating from 25 °C to 141 °C in approximately 60 °C increments, then cooled to 85 °C, with temperatures indicated on the right. Triangles indicate peaks characteristic of POSS crystallization centered at $q = 5.9 \pm 0.2$ nm^{-1}.

homopolymer (Fig. 3a) at $q = 6.1$ nm^{-1}, 8.1 nm^{-1}, and 9.0 nm^{-1}. This indicates that the POSS block packs into a rhombohedral crystal structure as was the case for POSS homopolymer. Heating the sample to 85 °C results in peaks at $q = 5.9$ nm^{-1} and 7.9 nm^{-1}. The relative locations of these peaks are similar to the peaks obtained at 25 °C indicating that the POSS-rich microphase is crystalline at temperatures between 25 and 85 °C. The size of the unit cell at 85 °C is slightly larger than that at 25 °C. Heating the sample further to 113 °C results in significant broadening of the peak at $q = 5.9$ nm^{-1} while the peak at $q = 7.9$ nm^{-1} remains more-or-less unchanged. This suggests that some planes in the POSS crystal structure disorder more readily than others as the melting transition is approached [10]. The scattering profile at 141 °C has one broad scattering peak that we attribute to the molten POSS-rich microphase. When the sample is cooled from 141 °C to 85 °C, the first peak centered at $q = 5.9$ nm^{-1} sharpens, and the second peak at $q = 7.8$ nm^{-1} reappears, signifying POSS recrystallization. The WAXS profile at 85 °C taken upon cooling is qualitatively similar to the profile at 85 °C upon heating, indicating thermoreversibility of the transition.

WAXS profiles of PEO-POSS(5–2) $r = 0.02$ (Fig. 3c) follow the expected trend: rhombohedral crystals are obtained at 25 °C and 85 °C melt when the sample is heated to 141 °C. WAXS profiles of PEO-POSS(10–4) $r = 0.02$ (Fig. 3d) also show rhombohedral crystals at 25 °C and 85 °C. However, weak signatures of crystallinity are also obtained at 141 °C.

The scattering patterns in Fig. 3a-d indicate that the presence of the PEO block does not impede crystallization of the POSS block [32]. Further, the addition of salt does not disrupt the POSS block crystallization.

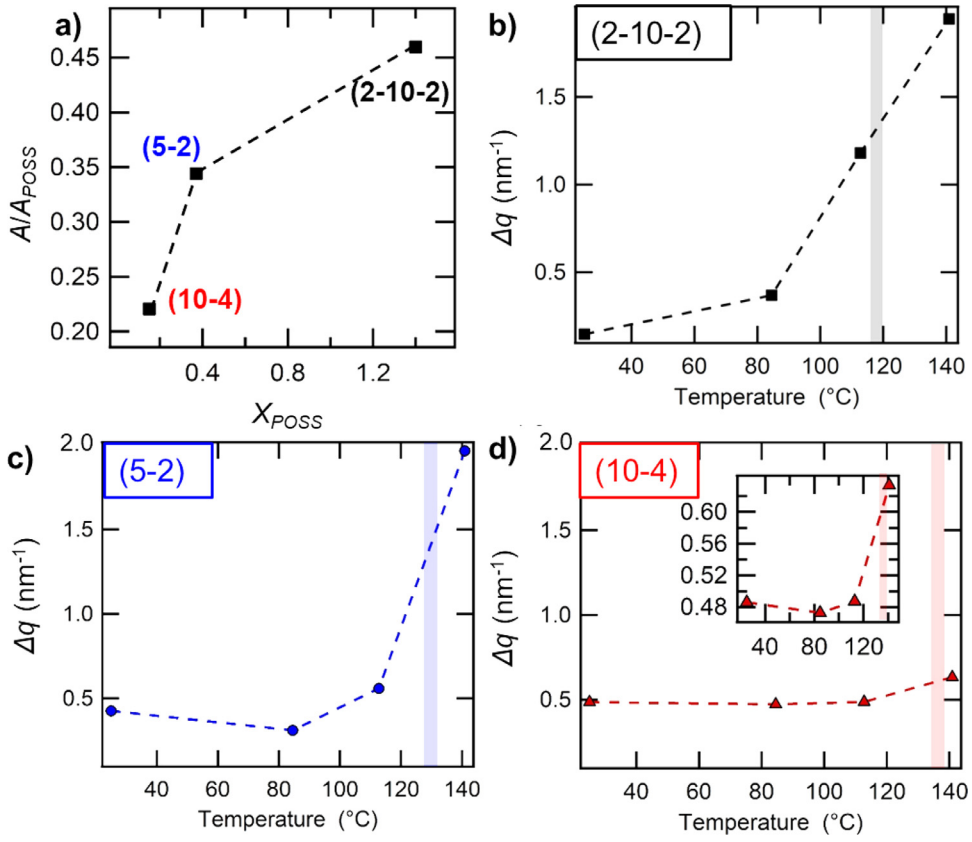

Fig. 4

Agreement between DSC and WAXS experiments in copolymer/salt mixtures at salt concentration $r = 0.02$. a) WAXS peak area at 85 °C divided by neat POSS homopolymer, A/A_{POSS} centered at $q = 5.9 \pm 0.2$ nm^{-1} versus relative percent crystallinity of the POSS domain (X_{POSS}). (b-d) Full width at half maximum (Δq) of WAXS peak centered at $q = 5.9 \pm 0.2$ nm^{-1} upon heating from 25 to 141 °C in each copolymer/salt mixture: b) POSS-PEO-POSS(2–10–2), c) PEO-POSS(5–2), and d) PEO-POSS(10–4). The shaded bar represents T_m obtained by DSC experiments.

Fig. 4a shows the correlation between WAXS and DSC experiments. The x-axis shows the relative percent crystallinity of the POSS microdomains, X_{POSS}, defined as $X_{POSS} = \Delta H_m w_{POSS}{}^{-1} \Delta H_{POSS}{}^{-1}$, where w_{POSS}, the weight fraction of the POSS block, is 0.27 for all copolymers. ΔH_m and ΔH_{POSS} are the POSS domain enthalpy of melting in the copolymer/salt mixture and the POSS homopolymer, respectively. The y-axis is the area under the WAXS peak centered around $q = 5.9 \pm 0.2$ nm^{-1}, A, normalized by the area under the neat POSS homopolymer WAXS peak, A_{POSS}, at 85 °C obtained during the heating scan. Fig. 4a demonstrates a correlation between A/A_{POSS} and X_{POSS}. POSS-PEO-POSS(2–10–2) exhibits the highest crystallinity as measured by either the magnitude of A/A_{POSS} or X_{POSS}. Note that X_{POSS} is greater than unity indicating that the POSS-rich microphases in POSS-PEO-POSS(2–10–2) contain less of the amorphous phase than POSS homopolymer.

Figs. 4b-d exhibit the full width at half maximum of the WAXS peak at $q = 5.9 \pm 0.2$ nm^{-1}, Δq, versus temperature between $25 < T < 141$ °C in each copolymer/salt mixture shown in Fig. 3b-d. The broadening of this peak (i.e., increase in Δq) indicates the POSS melting transition. Each figure also shows the POSS block melting transition temperature, T_m, obtained by DSC as a vertical bar. There is good correlation between the WAXS and DSC signatures of melting in Figs. 4b and c. We note that the peak broadening at the transition is more abrupt in PEO-POSS(5–2) (Fig. 4c) as compared to POSS-PEO-POSS(2–10–2) (Fig. 4b).

Fig. 4d demonstrates that PEO-POSS(10–4) $r = 0.02$ Δq is insensitive to temperature across the temperature range as compared to POSS-PEO-POSS(2–10–2) (Fig. 4b) and PEO-POSS(5–2) (Fig. 4c). However, the inset in Fig. 4d shows that Δq increases slightly from 0.48 nm^{-1} to 0.64 nm^{-1} upon heating from 113 °C to 141 °C. We postulate that the POSS domain is not entirely melted in PEO-POSS(10–4)/salt mixture at 141 °C, though the DSC thermogram indicates $T_m = 134.8$ °C. The disagreement between WAXS and DSC arises because of the lack of a sharp, well-defined melting point for the POSS block. Broad melting transitions are characteristic of semicrystalline block copolymers [39–41].

Crystallite size (L_{cry}) is inversely related to peak broadening as demonstrated by Scherrer's equation represented in reciprocal space, $L_{cry} = 2\pi K/\Delta q$, where K is the Scherrer constant and has a value of 0.9 and Δq is the measurement of the full width at half maximum of the WAXS peak [38]. Fig. 4b-d demonstrates L_{cry} decreases with increasing temperature in all three systems.

3.2 Effect of temperature

In Fig. 5a, SAXS intensity, $I(q)$, in POSS-PEO-POSS(2–10–2) $r = 0.02$ sample is plotted as a function of q, at selected temperatures upon cooling between 132 °C and 75 °C. The sample shows reversibility

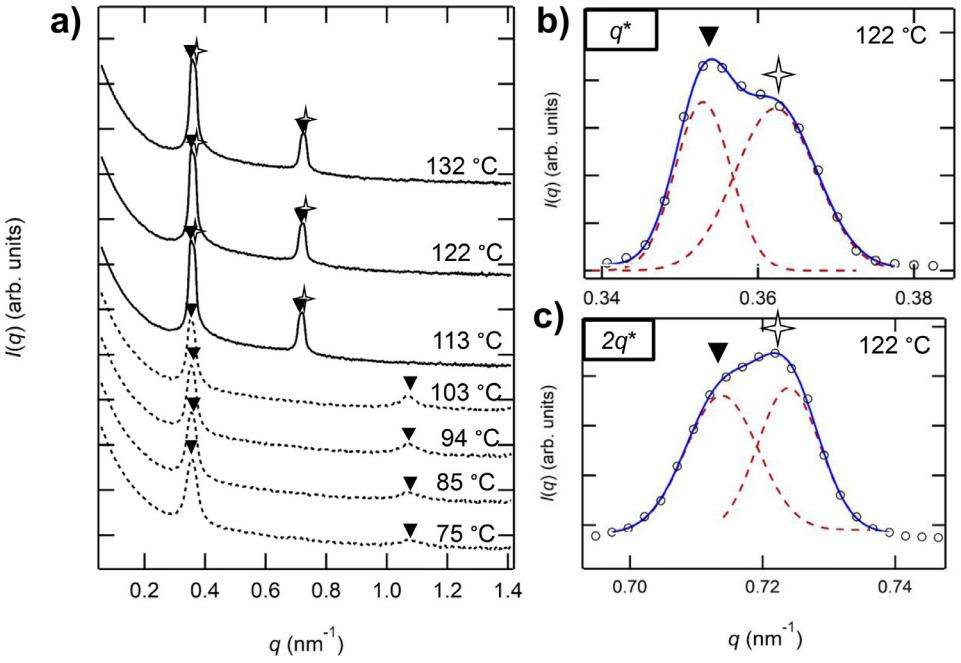

Fig. 5

a) SAXS intensity is plotted as a function of the magnitude of the scattering vector, q, in POSS-PEO-POSS(2–10–2) at $r = 0.02$. Solid lines indicate amorphous POSS block, dashed lines indicate semicrystalline POSS block. Scans are performed upon cooling from 132 °C to 75 °C in approximately 10 °C increments with temperatures indicated on the right. Expanded peaks at 122 °C are shown in the vicinity of a) $q = q^*$, and b) $q = 2q^*$. ▼and ✧ indicate peaks characteristic of lamellae ($q = q^*, 2q^*, 3q^*$) and coexisting lamellae respectively. The data in a) were reported in ref [25].

of phase transitions upon heating and cooling (heating scans not shown for brevity). Dashed scattering profiles indicate scans taken at $T < T_c$ (*i.e.*, the POSS block is semicrystalline), and solid scattering profiles are scans taken at $T > T_c$ (*i.e.*, the POSS block is amorphous). At 75 °$C \leq T \leq$ 103 °C, the POSS block is semicrystalline and the SAXS pattern reveals two peaks at $q = q^* = 0.35 \pm 0.01$ nm^{-1} and $q = 3q^*$, denoted by triangles, indicating the presence of alternating PEO/salt-rich and POSS-rich lamellae layers (*LAM*). The reason for the suppression of the expected scattering peak at $q = 2q^*$ remains to be established. It is possible that the presence of both amorphous and semicrystalline POSS microdomains are responsible for this observation.

The shapes of the SAXS peaks at temperatures between 113 and 132 °C in Fig. 5a are complex. In Fig. 5b, we show representative background subtracted SAXS profiles in the vicinity of the primary peak on an expanded scale (122 °C). This profile is consistent with the presence of two overlapping peaks. The SAXS data in Fig. 5b, shown as markers, were fit to a sum of two Lorentzian peaks. The solid curve through the data in Fig. 5b shows the fit and the two peaks are shown in red underneath the scattering data. We refer to the peak positions as $q_1{}^*$ and $q_2{}^*$. In Fig. 5c, we show background subtracted 122 °C SAXS profiles in the vicinity of the second order peaks on an expanded scale. This profile also indicates the presence of two overlapping peaks. The triangles and star symbols represent $2q_1{}^*$ and $2q_2{}^*$, the expected locations of second order peaks corresponding to the two primary peaks identified in Fig. 5b. The consistency of the analysis in Figs. 5b and c indicate the presence of two coexisting lamellar phases (*LAM*/*LAM*) with two different domain spacings: 17.3 nm and 17.8 nm. This coexistence is seen consistently at temperatures above T_c; the peaks obtained at temperatures below T_c are consistent with the presence of a single, conventional lamellar phase. (Some aspects of the morphology of POSS-PEO-POSS(2–10–2) $r = 0.02$ were reported in ref [25]. A detailed analysis of the shapes of the SAXS peaks was not included in ref [25].)

PEO-POSS(5–2) $r = 0.02$ SAXS scans are shown in Fig. 6a . Dashed scattering profiles indicate scans taken at $T < T_c$ (*i.e.*, the POSS block is semicrystalline), and solid scattering profiles are scans taken at $T > T_c$ (*i.e.*, the POSS block is amorphous). The scattering profiles below 94 °C exhibit a single, broad peak at $q = q^*$, a standard signature of a disordered phase (*DIS*) [1,42]. However, the POSS-rich concentration fluctuations are semicrystalline, and this may complicate interpretation of the scattering profiles. We address this point shortly. The emergence of two higher order peaks at $q = 2q^*$ and $q = 3q^*$ in the SAXS profiles at 103 °C indicate a *DIS* to *LAM* transition at $T = 98.5 \pm 5$ °C. The transition temperature is in good agreement with T_c determined by DSC (95 °C).

The scattering profiles at 122 °C and 132 °C exhibit a sharp peak superposed on the broad lamellar peak at $q = q^*$ seen in the scans taken at temperatures between 103 °$C < T <$ 113 °C. The background subtracted SAXS profiles in the vicinity of the primary peak on an expanded scale at 132 °C are shown in Fig. 6b. SAXS data in Fig. 6b, shown as markers, were fit to a sum of 1 Lorentzian peak, indicated in solid red, and 1 Gaussian peak, indicated in solid green. The solid blue curve through the scattering data in Fig. 5b shows the fit. The overlapping peaks indicate the presence of one weakly ordered lamellar phase coexisting with a well-

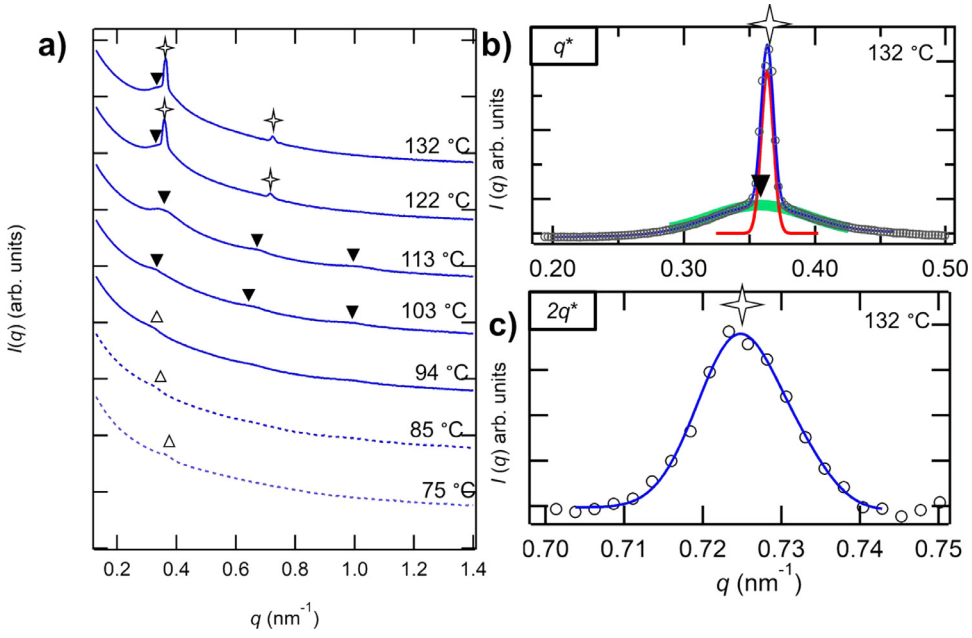

Fig. 6

a) SAXS intensity is plotted as a function of the magnitude of the scattering vector, q, in PEO-POSS(5–2) at $r = 0.02$. Solid lines indicate amorphous POSS block, dashed lines indicate semicrystalline POSS block. Scans are performed upon cooling from 132 °C to 75 °C in approximately 10 °C increments with temperatures indicated on the right. ▼, ✧, and △ indicate peaks characteristic of lamellae ($q = q^*, 2q^*, 3q^*$), coexisting lamellae, and disorder ($q = q^*$). Peaks in the vicinity of $q = q^*$ and $2q^*$ are expanded in b) and c) at 132 °C. The data in a) were reported in ref [23].

ordered lamellar phase, *LAM*/*LAM*, with two different domain spacings: 17.6 nm and 17.3 nm respectively. Fig. 6c shows the scattering data in the vicinity of $q = 2q^*$ at 132 °C. The data is fit to one Gaussian peak, shown as a blue curve. We postulate that the well-ordered *LAM* peak suppresses the weak, broad lamellar peak seen between 103 °C < T < 113 °C. Unlike the sample in Fig. 5a-c, the sample in Fig. 6a-c undergoes a *LAM* to *LAM*/*LAM* at a temperature 33 °C above T_c.

The results and error of all peak fittings demonstrated in Figs. 5-7 are shown in the Supporting Information, Table S3.

PEO-POSS(10–4) $r = 0.02$ SAXS profiles in Fig. 7a indicate a single Gaussian peak at $q = q^*$ at 84 °$C \leq T \leq$ 113 °C, a signature of *DIS*. This peak appears more well-defined than the *DIS* PEO-POSS(5–2) sample (Fig. 6a). At 122 °C, we see the emergence of overlapping peaks in the vicinity of $q = q^*$. The first, small peak is apparent at $q = 0.25$ nm^{-1}, and the second, more well-defined peak is centered around $q = 0.28$ nm^{-1}. We call these peaks $q_{,1}^*$ and $q_{,2}^*$, respectively, and are shown in Fig. 7b. In order to discern the morphology of this sample, the SAXS data between $q = 0.4$ and 0.6 nm^{-1} is shown in Fig. 7c. A single, Gaussian peak is fit to the data, centered at $q = 0.49$ nm^{-1}. The location of the second peak is $2q_1^*$ and is also equal to $\sqrt{3}q_2^*$. We therefore conclude that the peaks seen at $q = q_{,1}^*$ and $2q_{,1}^*$ is indicative of a *LAM* phase, while the peaks at $q_{,2}^*$ and $\sqrt{3}q_{2^*}$ indicate a coexisting hexagonally packed cylinders phase (*CYL*). Thus, this sample transitions from *DIS* to coexisting *LAM*/*CYL* at 117.5 ± 4.5 °C. These coexisting phases are evident in the window 122 °$C \leq T \leq$ 141 °C. In a previous study, we have established *LAM*/*CYL* coexistence in PEO-POSS(5–2) $r = 0.08$ wherein the SAXS data were augmented by electron tomography [23].

3.3 Effect of salt concentration

Our discussion thus far has only included samples at salt concentration $r = 0.02$. We now expand our DSC analysis to the copolymers without salt and higher salt concentrations to understand the effect of r on the crystallization of the POSS block in all copolymer/salt mixtures. Fig. 8a shows the POSS block T_m and T_c versus r for all three copolymer systems and neat POSS homopolymer. We note the T_m is greatest and T_c is lowest in the POSS homopolymer as compared to all neat copolymers and copolymer/salt mixtures. The T_m result is not surprising as it indicates that the melting of POSS crystals is facilitated by microphase separation. The T_c result is a little more interesting, as it indicates that nucleation of POSS crystals is facilitated by microphase separation. In the POSS-PEO-POSS(2–10–2) system, T_m and T_c both slightly increase with increasing salt concentration. Similarly, PEO-POSS(5–2) samples T_c increases slightly, while T_m decreases slightly over the experimental salt concentration range. For these two systems, T_m, and T_c are relatively weak functions of salt concentration. On the other hand, in the PEO-POSS(10–4) samples, T_m and T_c both decrease substantially in the salt concentration range between $0 \leq r \leq 0.08$. At $r > 0.08$, the POSS block is completely amorphous (i.e. no melting or crystallization transitions are discernable in the DSC thermograms). The dashed line through T_c is the linear fit through the data and will be used in subsequent analysis to estimate T_c in PEO-POSS(10–4)/salt mixtures at $r > 0.08$. These results suggest that salt ions do not interact exclusively with PEO chains. (We did try to dissolve LiTFSI in POSS homopolymer but found that the two materials were immiscible.)

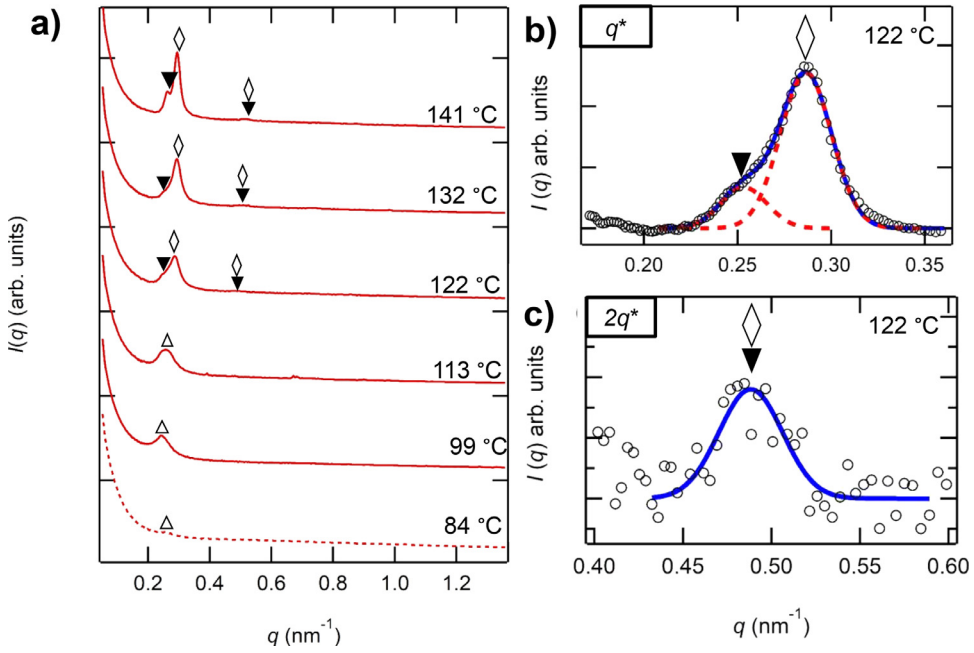

Fig. 7

a) SAXS intensity is plotted as a function of the magnitude of the scattering vector, q, in PEO-POSS(10–4) $r = 0.02$. Solid lines indicate amorphous POSS block, dashed lines indicate semicrystalline POSS block. Scans are performed upon cooling from 141 °C to 84 °C in approximately 10 °C increments with temperatures indicated on the right. ▼, △, and ♢, indicate peaks characteristic of lamellae ($q = q^*$, $2q^*$, $3q^*$), disorder ($q = q^*$), and hexagonally packed cylinders ($q = q^*$, $\sqrt{3}q^*$, $2q^*$). Peaks in the vicinity of $q = q^*$ and $2q^*$ are expanded in b) and c) at 122 °C.

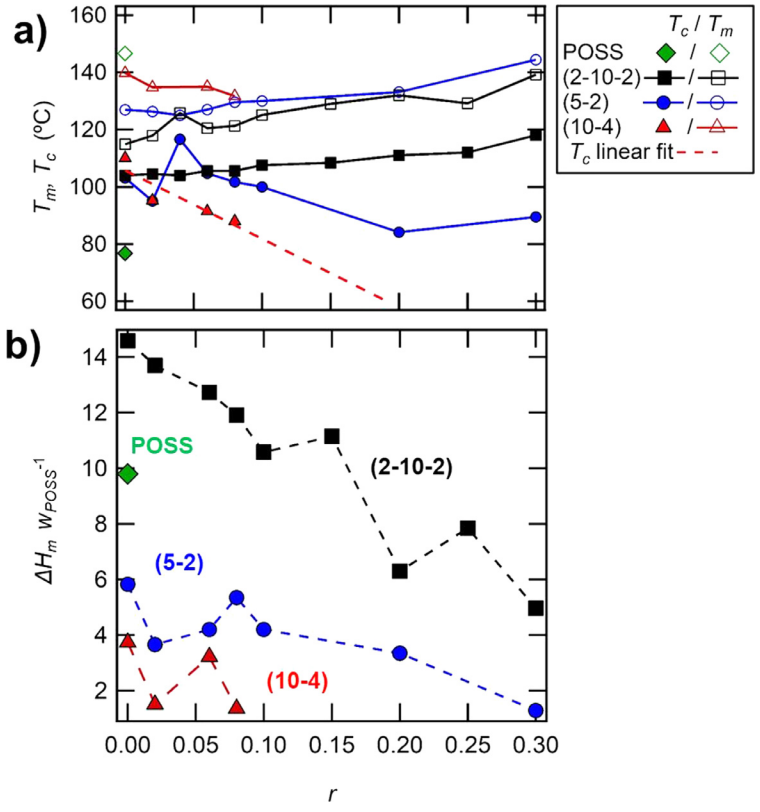

Fig. 8

Summary of all DSC experiments in neat POSS and POSS-PEO-POSS(2–10–2), PEO-POSS(5–2), and PEO-POSS(10–4)/salt mixtures. a) POSS block T_m and T_c b) $\Delta H_m w_{POSS}{}^{-1}$ as a function of salt concentration, r.

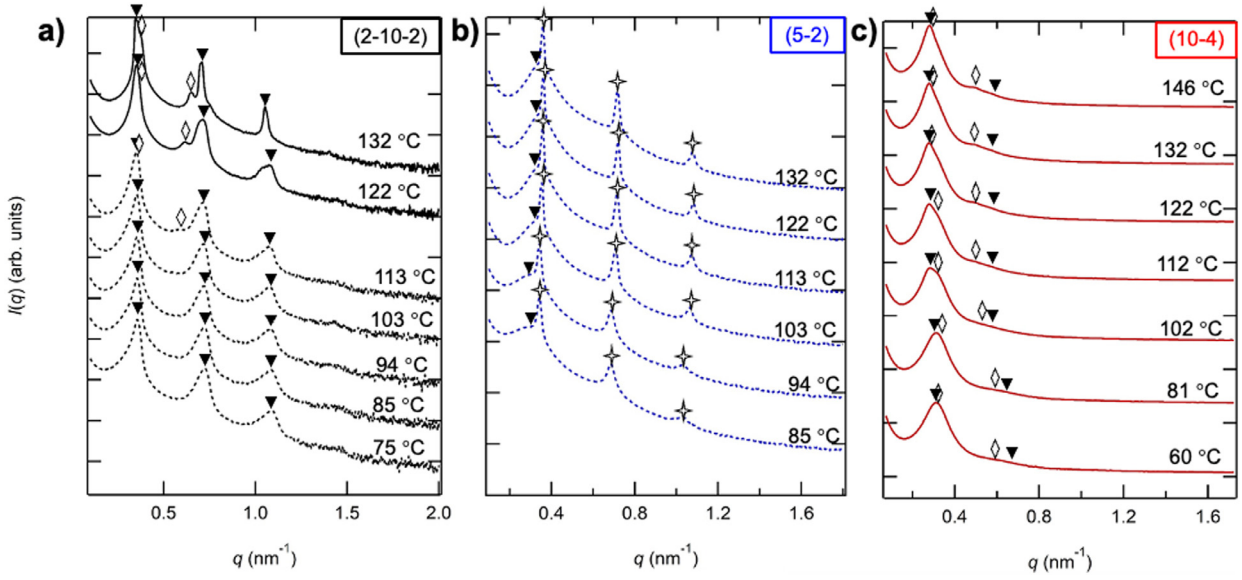

Fig. 9

SAXS scattering profiles of copolymers at $r = 0.20$ and 60 °C ≤ T ≤ 146 °C in a) POSS-PEO-POSS(2–10–2), b) PEO-POSS(5–2), and c) PEO-POSS(10–4). Profiles are shifted vertically. Solid lines indicate amorphous POSS block, dashed lines indicate samples containing a semicrystalline POSS block. Temperatures are indicated on the right. ▼, ✧, and ◊ indicate peaks characteristic of lamellae ($q = q^*$, $2q^*$, $3q$), coexisting lamellae, and hexagonally packed cylinders ($q = q^*$, $\sqrt{3}q^*$, $2q^*$).

Fig. 8b shows the enthalpy of POSS block melting normalized by weight percent of POSS, $\Delta H_m w_{POSS}^{-1}$ as a function of r. All three copolymer/salt mixtures exhibit a decrease in $\Delta H_m w_{POSS}^{-1}$ with increasing r, indicating weaker POSS block crystallization at higher salt concentrations. Surprisingly, the POSS block in the POSS-PEO-POSS(2–10–2) system appears more strongly crystalline than neat POSS homopolymer over a large range of salt concentrations, $0 \leq r \leq 0.15$. Above $r = 0.15$, $\Delta H_m w_{POSS}^{-1}$ of POSS-PEO-POSS(2–10–2)/salt mixtures decreases below that of the neat POSS homopolymer. At all salt concentrations, the triblock copolymer/salt mixtures exhibit stronger POSS crystallinity than both diblock copolymer/salt mixtures. PEO-POSS(10–4)/salt mixtures exhibits the weakest POSS block crystallinity of all three copolymers up to $r = 0.08$ (above this salt concentration, the POSS block is amorphous).

Fig. 9a shows SAXS profiles of POSS-PEO-POSS(2–10–2) $r = 0.20$ at a temperature range 75 °C ≤ T ≤ 132 °C, obtained during cooling. The dashed lines indicate SAXS profiles wherein the POSS block in the sample is semicrystalline (i.e. $T < T_c$) in the temperature regime 75 °C ≤ T ≤ 113 °C. The SAXS profiles show clear peaks at $q = q^*$, $2q^*$, and $3q^*$, indicative of well-ordered *LAM*, denoted by filled triangles. The solid line SAXS profiles indicate measurements wherein the POSS block is amorphous (*i.e.*, $T > T_c$) between 122 °C ≤ T ≤ 132 °C. At 112 °C, we see the emergence of a second primary peak at $q = q_{,2}^*$. Additionally, a broad peak appears at $q = \sqrt{3}q_{,2}^*$, a signature of *CYL* phase coexisting with the *LAM*. In the profiles at 122 °C and 132 °C, the peaks representative of *LAM* as well as the peaks representative of *CYL* sharpen and grow with intensity. Fig. 7a shows the POSS-PEO-POSS(2–10–2) $r = 0.20$ sample undergoes an order-order transition from *LAM* to *LAM*/*CYL* upon heating at 117.5 ± 4.5 °C, coinciding with T_c measured by DSC.

Fig. 9b shows SAXS profiles of PEO-POSS(5–2) at the same salt concentration as Fig. 9a ($r = 0.20$) at a temperature range 85 °C ≤ T ≤ 132 °C, obtained during a cooling run. The highest temperature is below the melting temperature of the POSS block ($T_m = 133.1$ °C). Thus, the POSS block is semicrystalline throughout the accessible temperature regime. We see *LAM* characteristic peaks in all profiles (i.e. peaks centered at $q = q^*$, $2q^*$), denoted by triangles. The peaks grow in intensity and sharpen with increasing temperature. However, in all measurements, we note the appearance of a broad, Gaussian peak coexisting with the ordered *LAM* peaks. These SAXS peaks are qualitatively similar to those obtained at $r = 0.02$ (Fig. 6a). We thus posit the presence of two coexisting *LAM* phases (*LAM*/*LAM*).

Fig. 9c shows SAXS data for PEO-POSS(10–4) $r = 0.20$ at a temperatures 60 °C ≤ T ≤ 146 °C (the POSS block is amorphous at this salt concentration in this sample). We see *LAM* characteristic peaks in all profiles (i.e. peaks centered at $q = q^*$ and $2q^*$) as well as coexisting *CYL* characteristic peaks (*i.e.* peaks centered at $q = q_{,2}^*$ and $\sqrt{3}q_{,2}^*$). Thus, this sample contains an ordered phase of *LAM*/*CYL* with two different domain spacings, similar to POSS-PEO-POSS(2–10–2)/salt mixture (Fig. 7a) at 122 °C ≤ T ≤ 132 °C.

Fig. 9 demonstrates that only *LAM* are seen in crystalline samples (dashed curves in Fig. 9) as predicted by Whitmore and Noolandi [7]. Curved interfaces are only seen in samples above T_c as might be expected of asymmetric copolymer/salt mixtures ($0.76 \leq f_{EO/LiTFSI} \leq 0.85$). However, *CYL* always coexist with *LAM* despite the fact the PEO and POSS blocks are both amorphous.

The effect of added salt on the morphology is shown in Fig. 10a-c, where SAXS data is shown in each system at varied salt concentrations but at constant temperature. Fig. 10a shows data for the POSS-PEO-POSS(2–10–2)/salt mixtures at 132 °C. All samples are ordered at this temperature. In the neat sample ($r = 0$),

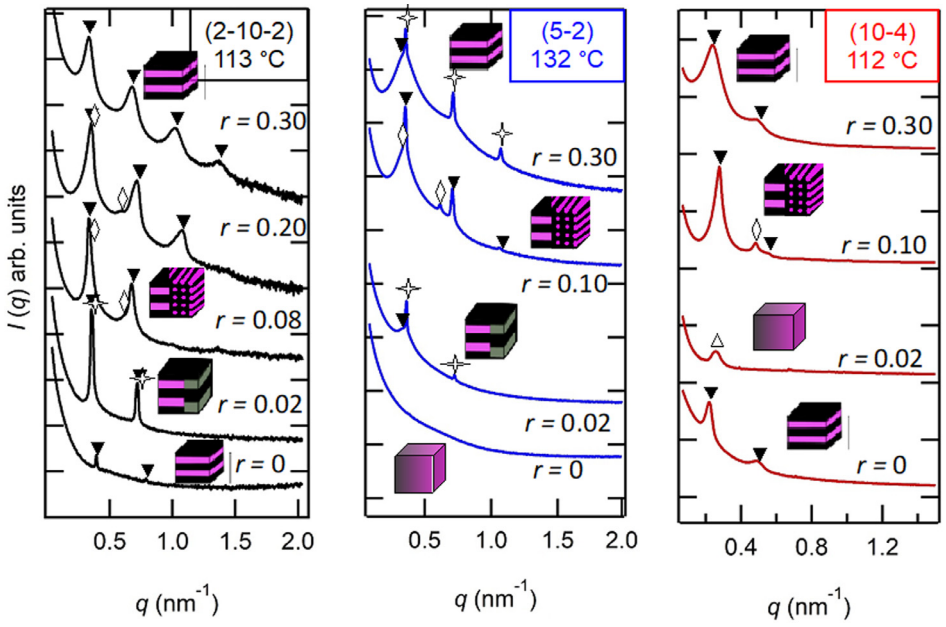

Fig. 10

SAXS scattering profiles of copolymer/salt mixtures at constant temperature and varied salt concentration, $0 \leq r \leq 0.30$. a) POSS-PEO-POSS(2–10–2), b) PEO-POSS(5–2), and c) PEO-POSS(10–4). Profiles are shifted vertically. Salt concentration are indicated on the right. ▼, ✧, and ◊ indicate peaks characteristic of lamellae ($q = q^*$, $2q^*$, $3q$), coexisting lamellae, and hexagonally packed cylinders ($q = q^*$, $\sqrt{3}q^*$, $2q^*$).

a *LAM* phase is obtained. At $r = 0.02$, *LAM/LAM* coexistence is obtained, and the peaks are much sharper than the neat sample. Increasing the salt concentration to $r = 0.08$ results in the emergence of additional scattering peaks at $q = q_{,2}{}^*$ and $\sqrt{3}q_{,2}{}^*$ that are superimposed on the scattering profile of the lamellar phase, standard signatures of *CYL*. Increasing salt concentration further to $r = 0.20$ results in the sharpening and increased intensity of both the *LAM* and *CYL* peaks. Finally, the highest salt concentration $r = 0.30$ results in *LAM*.

PEO-POSS(5–2)/salt mixtures at 132 °C are shown in Fig. 10b. The neat sample is *DIS*, while all salt containing samples are ordered. At low salt concentration, $r = 0.02$ the profile indicates *LAM/LAM*. Increasing the salt concentration to $r = 0.10$ results in *LAM/CYL* coexistence. Increasing salt concentration further to $r = 0.30$ results in *LAM/LAM* coexistence.

PEO-POSS(10–4)/salt mixtures at 112 °C are shown in Fig. 10c. The neat sample is *LAM* while the $r = 0.02$ is *DIS*. Increasing the salt concentration to $r = 0.10$ results in *LAM/CYL*. Increasing salt concentration further to $r = 0.30$ results in a *LAM* phase as seen in POSS-PEO-POSS(2–10–2) $r = 0.30$.

3.4 Phase diagram

Fig. 11 summarizes the morphology of the block copolymer electrolytes and the semicrystalline properties of the POSS-rich microphase in the temperature range $70\ °C \leq T \leq 140$ °C and salt concentration range $0 \leq r \leq 0.30$. The different morphologies, *LAM, DIS, LAM/CYL*, and *LAM/LAM* are shaded in gray, yellow, and hatched green and hatched gray regions respectively. T_m (triangles) and T_c (squares) are plotted on top of the morphology data. The colors of T_m and T_c markers indicate the magnitude of $\Delta H_m w_{POSS}{}^{-1}$, as indicated by the accompanying color scale.

The POSS-PEO-POSS(2–10–2) system (Fig. 11a) is ordered at all temperatures and salt concentrations. The neat polymer is *LAM* throughout the accessible temperature window (both above and below T_c). The addition of salt results in the emergence of a wide *LAM/LAM* window at high temperature. The rest of the phase diagram is dominated by *LAM* morphology with a wide window of *LAM/CYL* above T_c. Phase transitions occur close to T_c in all salt-containing samples. It is evident that phase coexistence is not an intrinsic property of the copolymer but is induced by the addition of salt.

In the POSS-PEO-POSS(5–2) system (Fig. 11b), small pockets of *DIS* appear. A *LAM* to *DIS* transition upon heating is seen in the neat block copolymer above T_c. A *DIS* phase is seen at $r = 0.02$ that form *LAM* upon heating. At higher temperatures, a coexisting phase of *LAM/LAM* appears. *LAM/LAM* is seen over a wide window giving way to *LAM/CYL* coexistence at intermediate salt concentrations and high temperatures above T_c. At $r = 0.20$ and 0.30, the *LAM/LAM* phase dominates. We note that all SAXS scans at these salt concentrations were performed at temperatures below the melting transition (*i.e.*, $T < T_m$). We also note that in phase coexistence is only seen in the salt-containing systems in POSS-PEO-POSS(5–2).

In the PEO-POSS(10–4) system (Fig. 11c), the neat polymer does not exhibit any transition and is *LAM* throughout the accessible temperature window. The addition of salt results in the stabilization of a wider *DIS* window than in PEO-POSS(5–2) system at low salt concentration and temperature. The rest of the phase diagram is ordered *LAM/CYL* and *LAM* at highest salt concentration ($r = 0.30$). Note that we only observe thermally driven phase transitions in copolymer/salt mixtures wherein the POSS block undergoes crystalline to amorphous transition with

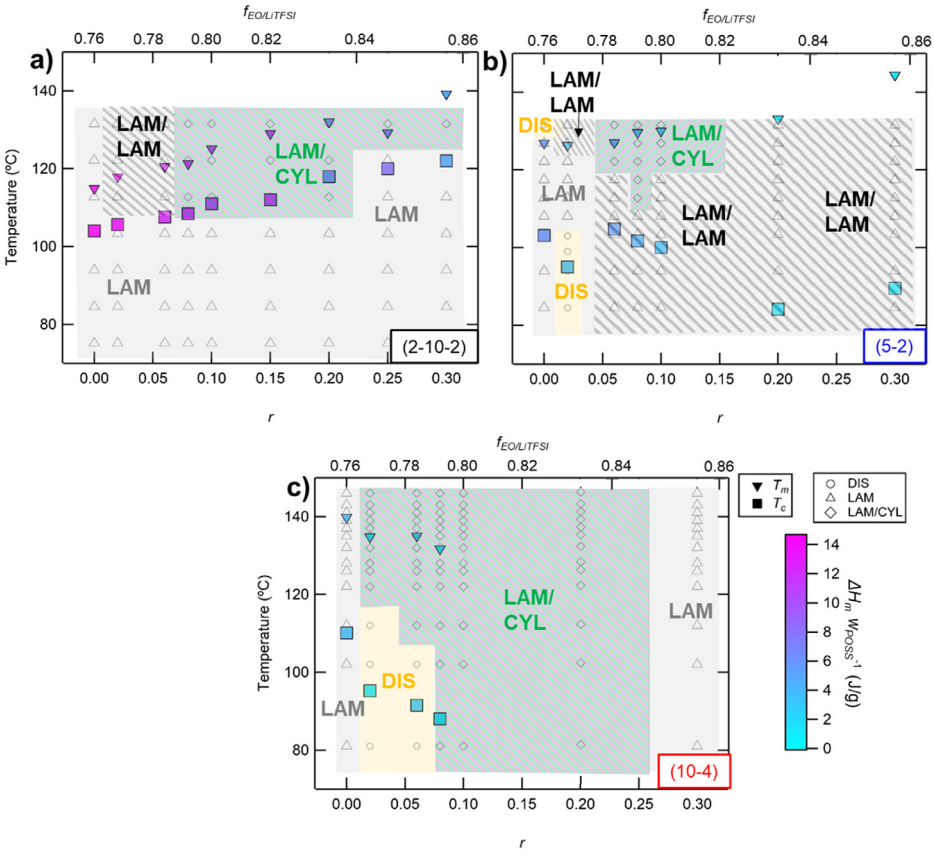

Fig. 11

Phase diagrams of a) POSS-PEO-POSS(2–10–2), b) PEO-POSS(5–2), and c) PEO-POSS(10–4)/ salt mixtures summarizing morphology data determined by SAXS as a function salt concentration, *r*, and temperature upon cooling. The top axis is the EO/LiTFSI volume fraction, $f_{EO/LiTFSI}$. The green hatched, gray, gray hatched, and yellow regions represent lamellae/hexagonally packed cylinders (*LAM/CYL*), lamellar (*LAM*), coexisting lamellar (*LAM/LAM*), and disordered (*DIS*) morphologies respectively. Melting (triangles) and crystallization (square) temperatures (T_m, T_c) are shown with color scale representing normalized enthalpy of melting, $\Delta H_m w_{POSS}{}^{-1}$.

the exception of $r = 0.08$, which lies at the border between the two regimes.

Fig. 11 demonstrates that POSS crystallization drives thermally driven phase transitions in all 3 systems. Phase transitions occur most closely to T_c in systems exhibiting greater $\Delta H_m w_{POSS}{}^{-1}$ (*i.e.*, T_c markers shown in pink) versus those with weaker POSS crystallinity (i.e., T_c markers shown in blue).

At 122 °C, all three systems exhibit *LAM/CYL* coexistence windows at intermediate salt concentrations. This is quantified in Fig. 12 where we estimate the fraction of *CYL* grains, f_{CYL}, as follows,

$$f_{CYL} = \frac{S_{\sqrt{3}q*}}{S_{\sqrt{3}q*} + S_{2q*}} \tag{6}$$

where $S_{\sqrt{3}q*}$ is the SAXS invariant centered around $q = \sqrt{3}q*$, and S_{2q*} is the SAXS invariant centered around $q = 2q^*$. f_{CYL} versus salt concentration is plotted in Fig. 12a-c. Each plot shows a clear maximum in f_{CYL} near the middle of the *LAM/CYL* coexistence window shown in Fig. 11a-c. While POSS-PEO-POSS(2–10–2)/salt exhibits a clear maximum in f_{CYL} at $r = 0.15$, both diblock copolymers exhibits peak f_{CYL} at $r = 0.08$. The relative amount of f_{CYL} is almost 95% at the maximum in PEO-POSS(10–4), which contains the largest *LAM/CYL* window. f_{CYL} is 60% at the maximum in POSS-PEO-POSS(2–10–2), which contains the second largest *LAM/CYL* window, and only 11% in PEO-POSS(5–2), which has the smallest *LAM/CYL* coexistence window.

Fig. 12d-f show the domain spacing, *d* of ordered morphologies, d_{LAM} and d_{CYL} at 122 °C, as a function of *r*. The variables $d_{LAM,I}$ and $d_{LAM,II}$ are assigned as the domain spacings of coexisting lamellae.

The d_{LAM} in neat POSS-PEO-POSS(2–10–2) is 19.8 nm. A large decrease in *d* is observed with the addition of a small amount of salt ($r = 0.02$); the two coexisting *LAM* phases have domains spacings of 17.3 nm and 17.8 nm. The *d* in the presence of salt is affected by two competing effects: increased segregation between the blocks will increase *d* while the specific solvation motif on PEO chains around Li^+ ions will cause a decrease in *d* [43]. The observed decrease suggests that solvation effects dominate despite of the low salt concentration. *d* increases rapidly with increasing salt, reaching a maximum of 21.5 nm at $r = 0.15$. This is the salt concentration at which f_{CYL} also exhibits a maximum; compare Figs. 12a and 12d. The sizes of the coexisting phases in POSS-PEO-POSS(2–10–2)/salt mixtures, appear to be codependent and within 1 nm between $0.02 \leq r \leq 0.20$ At $r = 0.20$, $d_{LAM} = d_{CYL}$, and at high

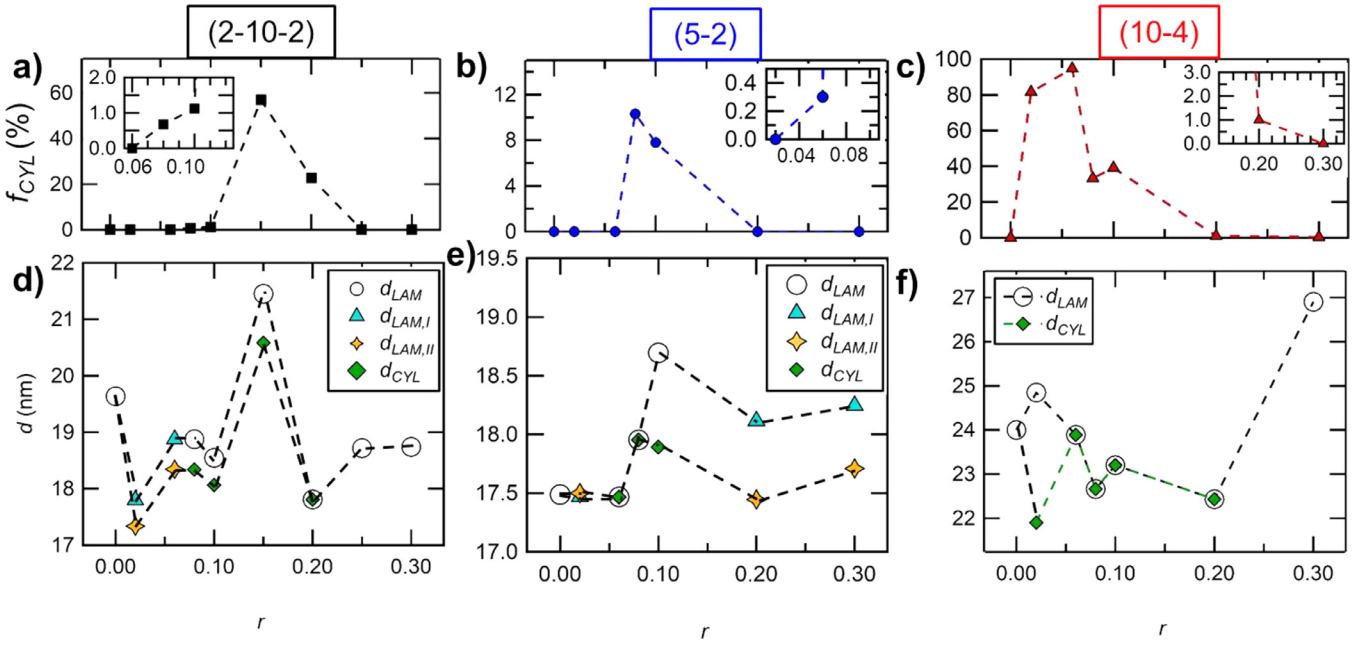

Fig. 12

Fraction cylinders (f_{CYL}) and domain spacing, d, of lamellae (d_{LAM}), hexagonally packed cylinders (d_{CYL}), and coexisting lamellae ($d_{LAM,I}$, $d_{LAM,II}$), versus salt concentration, r, at 122 °C in a,d) POSS-PEO-POSS (2–10–2) b,e) PEO-POSS(5–2) and c,f) PEO-POSS(10–4).

salt concentrations (i.e., $r > 0.20$), coexisting phases give way to a pure *LAM* phase.

The d of neat PEO-POSS(5–2) is smaller than that of neat POSS-PEO-POSS(2–10–2), as expected (Fig. 12e). The effect of added salt on d is less dramatic in PEO-POSS(5–2). However, many of the features observed in Figs. 12e are qualitatively similar to Fig. 12d. The d of coexisting phases are codependent and the peak in d_{LAM} occurs at $r = 0.10$, while the peak in d_{CYL} occurs at $r = 0.08$ (the same salt concentration at which a peak in f_{CYL} is observed (Fig. 12b)).

The d of neat PEO-POSS(10–4) is a factor of 1.4 larger than that of PEO-POSS(5–2), as expected from systems in the weak segregation limit (d is proportional to the square root of chain length). The addition of a small amount of salt ($r = 0.02$) leads to coexistence where d_{CYL} is more than 3 nm greater than d_{LAM}. At this salt concentration, it appears that the consequence of increased segregation is apparent in the cylinder phase while the consequence of ion solvation is apparent in the lamellar phase. At all other salt concentrations where coexistence is observed ($0.02 \leq r \leq 0.20$), the d of coexisting phases are codependent and indistinguishable. The domain spacing of the pure *LAM* phase at $r = 0.30$ is considerably larger than that of any of the other PEO-POSS(10–4) systems. We posit that the formation of coexisting phases relieves the chain stretching penalty associated with increased segregation.

In all three systems, the maximum in d_{CYL} occurs at the salt concentration for which we see the maximum of f_{CYL}.

In ref [24] we used the random phase approximation (RPA) to interpret scattering from disordered PEO-POSS/LiTFSI mixtures in terms of an effective Flory-Huggins interaction parameter, χ_{eff}. These data are revisited in Figure S8 in the SI in light of our recent understanding of the semicrystalline nature of the POSS block. With one exception, all of the samples analyzed using RPA were amorphous and thus the fits of χ_{eff} reported in ref [24] are entirely valid. Interestingly, the disordered sample that is below T_c as measured by DSC exhibits a χ_{eff} that is a smooth extrapolation as a function of temperature from data obtained from amorphous systems. The data as presented in Fig. 11 suggests that the crystallization of the POSS block is the most important driving force for phase separation, not the dependence of χ_{eff} on temperature and salt concentration.

4 Conclusion

In this paper, we elucidate the relationship between crystallization of the POSS block and self-assembly in a triblock copolymer, POSS-PEO-POSS, and two diblock copolymers, PEO-POSS, mixed with LiTFSI salt. In the copolymer/salt mixtures, the POSS block is semicrystalline and packs in a rhombohedral lattice, determined by DSC and WAXS. The relative percent crystallinity of the POSS block, determined by DSC, was greater in the triblock copolymer as compared to both diblock copolymers and the POSS homopolymer.

SAXS was used to determine the morphology of POSS-PEO-POSS and PEO-POSS/salt mixtures over a temperature range $60 \leq T \leq 140$ °C and $0 \leq r \leq 0.30$. Disorder or ordered phases with flat interfaces (*i.e.*, lamellae) are apparent in samples wherein the POSS block is semicrystalline. Pockets of POSS-rich cylinders form only in samples with amorphous POSS blocks and always coexist with lamellar grains. The copolymer/salt mixtures exhibit large windows of coexistence of lamellae and hexagonally packed cylinders, as well as coexisting lamellae with two different domain spacings over the experimental window. The correlation between POSS crystallization and phase transitions is greatest in systems wherein the POSS block exhibits the highest degree of crystallinity.

The phase diagrams shown in Fig. 11 are very different from other reports in the literature for two reasons: (1) the correlation between phase behavior and the crystallization of the POSS block, and (2) the presence of wide coexistence windows in the amorphous state that are not observed in the well-studied case of all-organic block copolymers.

In most theoretical phase diagrams of block copolymer/salt mixtures, the coexistence window that must lie between different ordered phases, due to the Gibbs Phase Rule, is ignored [4,44–48]. To our knowledge, the width of coexisting phases has only quantified for the case of symmetric lamellae, wherein the symmetry of both phases is assumed to be the same [49]. The presence of coexistence windows in all-organic copolymer/salt mixtures have been reported but are smaller as compared to the coexistence windows of the hybrid organic-inorganic/salt mixtures reported here [50,51].

In the absence of crystallization, self-consistent field theory (SCFT) predicts that increasing N suppresses the disordered phases [52,53]. We find that when we compare the neat diblock copolymers, we see the disappearance of the *DIS* phase with increasing chain length as we would expect from SCFT. However, in the diblock copolymer/salt mixtures, the *DIS* window in diblock copolymer with larger N is greater than in the smaller diblock copolymer. This result is inconsistent with predicted phase diagrams using both classical SCFT as well as ionic SCFT [18,44,45,47].

Matsen demonstrated in analogous diblock and triblock copolymers that the ordered phases in a theoretical phase diagram calculated by SCFT remains unchanged; however, the order-disorder phase boundary shifts to lower χN in triblock copolymers [21]. The neat triblock POSS-PEO-POSS(2-10-2) copolymer does not show *DIS* morphology, while the neat diblock PEO-POSS(5-2) copolymer does show *DIS* morphology, which is consistent with SCFT. [21,42,44].

Author contributions

The manuscript was written through contributions of all authors. All authors have given approval to the final version of the manuscript.

Declaration of Competing Interest

The authors declare that they have no known competing financial interests or personal relationships that could have appeared to influence the work reported in this paper.

Acknowledgment

This work was supported by the Assistant Secretary for Energy Efficiency and Renewable Energy, Office of Vehicle Technologies of the U.S. Department of Energy under Contract DE-AC02-05CH11231 under the Battery Materials Research Program. X-ray work performed at Advanced Light Source, which is a DOE Office of Science User Facility, was supported by Contract No. DE-AC02-05CH11231. X-ray work performed at the Stanford Synchrotron Radiation Light Source, a user facility at SLAC National Accelerator Laboratory, was supported by the U.S. Department of Energy, Office of Science, Office of Basic Energy Sciences under Contract No. DE-AC02-76SF00515. Work at the Molecular Foundry was supported by the Office of Science, Office of Basic Energy Sciences, of the U.S. Department of Energy under Contract No. DE-AC02-05CH11231. G.K.S. acknowledges funding from a National Science Foundation Graduate Student Research Fellowship.

Supplementary materials

Supplementary material associated with this article can be found, in the online version, at doi:10.1016/j.giant.2021.100055.

References

[1] L. Leibler, Theory of microphase separation in block copolymers, Macromolecules 13 (1980) 1602–1617, doi:10.1021/ma60078a047.

[2] P. Mansky, O.K.C. Tsui, T.P. Russell, Y. Gallot, Phase coherence and microphase separation transitions in diblock copolymer thin films, Macromolecules 32 (1999) 4832–4837, doi:10.1021/Ma990140x.

[3] K. Almdal, K.A. Koppi, F.S. Bates, K Mortensen, Multiple ordered phases in a block copolymer melt, Macromolecules 25 (1992) 1743–1751, doi:10.1021/ma00032a019.

[4] N.S. Wanakule, J.M. Virgili, A.A. Teran, Z.G. Wang, N.P. Balsara, Thermodynamic properties of block copolymer electrolytes containing imidazolium and lithium salts, Macromolecules 43 (2010) 8282–8289, doi:10.1021/ma1013786.

[5] H. Fischer, R. Weidisch, M. Stamm, H. Budde, S. Höring, The phase diagram of the system poly (styrene-block-n-butyl methacrylate), Colloid Polym. Sci. 278 (2000) 1019–1031, doi:10.1007/s003960000363.

[6] G. Gee, P.J. Flory, Statistical thermodynamics of semi-flexible chain molecules, Proc. R Soc. A Math. Phys. Eng. Sci. 234 (1956) 60–73, doi:10.1098/rspa.1956.0015.

[7] M. Douglas Whitmore, J Noolandi, Theory of crystallizable block copolymer blends, Macromolecules 21 (1988) 1482–1496, doi:10.1021/ma00183a044.

[8] L. Zhu, S.Z.D. Cheng, B.H. Calhoun, Q. Ge, R.P. Quirk, E.L. Thomas, B.S. Hsiao, F. Yeh, B. Lotz, Crystallization temperature-dependent crystal orientations within nanoscale confined lamellae of a self-assembled crystalline - Amorphous diblock copolymer, J. Am. Chem. Soc. 122 (2000) 5957–5967, doi:10.1021/ja000275e.

[9] A. Keller, M.J. Machin, Oriented crystallization in polymers, J. Macromol. Sci. Part B 1 (1967) 41–91, doi:10.1080/00222346708212739.

[10] K. Wu, M. Huang, K. Yue, C. Liu, Z. Lin, H. Liu, W. Zhang, C.H. Hsu, A.C. Shi, Zhang W Bin, et al., Asymmetric giant "bolaform-like" surfactants: precise synthesis, phase diagram, and crystallization-induced phase separation, Macromolecules 47 (2014) 4622–4633, doi:10.1021/ma501017e.

[11] P. Rangarajan, R.A. Register, D.H. Adamson, L.J. Fetters, W. Bras, S. Naylor, A.J. Ryan, Dynamics of structure formation in crystallizable block copolymers, Macromolecules 28 (1995) 1422–1428, doi:10.1021/ma00109a013.

[12] M. Gervais, B. Gallot, Phase diagram and structural study of polystyrene - poly(ethy1ene oxide) block copolymers, 1, Die Makromol. Chemie 178 (1973) 157–178.

[13] P. Rangarajan, R.A. Register, L.J. Fetters, Morphology of semicrystalline block copolymers of ethylene-(ethylene-alt-propylene), Macromolecules 26 (1993) 4640–4645, doi:10.1021/ma00069a034.

[14] Bruce P.G., Gray F.M. *Polymer electrolytes II: physical principles*. (1995).

[15] D. Devaux, D. Glé, T.N.T. Phan, D. Gigmes, E. Giroud, M. Deschamps, R. Denoyel, R. Bouchet, Optimization of block copolymer electrolytes for lithium metal batteries, Chem. Mater. 27 (2015) 4682–4692, doi:10.1021/acs.chemmater.5b01273.

[16] O. Oparaji, S. Narayanan, A. Sandy, S. Ramakrishnan, D. Hallinan, Structural dynamics of strongly segregated block copolymer electrolytes, Macromolecules 51 (2018) 2591–2603, doi:10.1021/acs.macromol.7b01803.

[17] F.S. Bates, G.H. Fredrickson, Block copolymer thermodynamics: theory and experiment, Annu. Rev. Phys. Chem. 41 (1990) 525–557, doi:10.1146/annurev.physchem.41.1.525.

[18] A.M. Mayes, La Olvera De, M. Cruz, Concentration fluctuation effects on disorder-order transitions in block copolymer melts, J. Chem. Phys. 95 (1991) 4670–4677, doi:10.1063/1.461736.

[19] J.R.M. Giles, F.M. Gray, J.R. MacCallum, C.A. Vincent, Synthesis and characterization of ABA block copolymer-based polymer electrolytes, Polymer (Guildf) 28 (1987) 1977–1981, doi:10.1016/0032-3861(87)90309-0.

[20] C.C. Lin, S.V. Jonnalagadda, P.K. Kesani, H.J. Dai, N.P. Balsara, Effect of molecular structure on the thermodynamics of block copolymer melts, Macromolecules 27 (1994) 7769–7780, doi:10.1021/ma00104a035.

[21] M.W. Matsen, Equilibrium behavior of asymmetric ABA triblock copolymer melts, J. Chem. Phys. 113 (2000) 5539–5544, doi:10.1063/1.1289889.

[22] K. Timachova, G.K. Sethi, R. Bhattacharya, I. Villaluenga, N.P. Balsara, Ion diffusion across a disorder-to-order phase transition in a poly(ethylene oxide)-b -poly(silsesquioxane) block copolymer electrolyte, Mol. Syst. Des. Eng. (2019), doi:10.1039/c8me00077h.

[23] G.K. Sethi, X. Jiang, R. Chakraborty, W.S. Loo, I. Villaluenga, N.P. Balsara, Anomalous self-assembly and ion transport in nanostructured organic–inorganic solid electrolytes, ACS Macro Lett. (2018) 1056–1061, doi:10.1021/acsmacrolett.8b00583.

[24] G.K. Sethi, H.Y. Jung, W.S. Loo, S. Sawhney, M.J. Park, N.P. Balsara, I. Villaluenga, Structure and thermodynamics of hybrid organic-inorganic diblock copolymers with salt, Macromolecules 52 (2019) 3165–3175, doi:10.1021/acs.macromol.9b00042.

[25] Chakraborty S., Jiang X., Ho Z.J., Sethi G.K., Zhu C., Balsara N.P. Reversible changes in the grain structure and conductivity in a block copolymer electrolyte. (2020) doi:10.1021/acs.macromol.0c00466

[26] A.A. Teran, N.P. Balsara, Thermodynamics of block copolymers with and without salt, J. Phys. Chem. B 118 (2014) 4–17, doi:10.1021/jp408079z.

[27] D.M. Pesko, K. Timachova, R. Bhattacharya, M.C. Smith, I. Villaluenga, J. Newman, N.P. Balsara, Negative transference numbers in poly(ethylene oxide)-based electrolytes, J. Electrochem. Soc. 164 (2017) E3569–E3575, doi:10.1149/2.0581711jes.

[28] Ilavsky J. Nika, Software for two-dimensional data reduction, J. Appl. Crystallogr. 45 (2012) 324–328, doi:10.1107/S0021889812004037.

[29] H. Liu, J. Luo, W. Shan, D. Guo, J. Wang, C.H. Hsu, M. Huang, W. Zhang, B. Lotz, Zhang W Bin, et al., Manipulation of self-assembled nanostructure dimensions in molecular janus particles, ACS Nano 10 (2016) 6585–6596, doi:10.1021/acsnano.6b01336.

[30] J.D. Lichtenhan, Y.A. Otonari, M.J. Carr, Linear hybrid polymer building blocks: methacrylate-functionalized polyhedral oligomeric silsesquioxane monomers and polymers, Macromolecules 28 (1995) 8435–8437, doi:10.1021/ma00128a067.

[31] J. Miao, L. Cui, H.P. Lau, P.T. Mather, L. Zhu, Self-assembly and chain-folding in hybrid coil-coil-cube triblock oligomers of polyethylene-b-poly(ethylene oxide)-b-polyhedral oligomeric silsesquioxane, Macromolecules 40 (2007) 5460–5470, doi:10.1021/ma070770w.

[32] L. Zheng, A.J. Waddon, R.J. Farris, E.B. Coughlin, X-ray characterizations of polyethylene polyhedral oligomeric silsesquioxane copolymers, Macromolecules 35 (2002) 2375–2379, doi:10.1021/ma011855e.

[33] A.J. Waddon, L. Zheng, R.J. Farris, E.B. Coughlin, Nanostructured polyethylene-POSS copolymers: control of crystallization and aggregation, Nano Lett. 2 (2002) 1149–1155, doi:10.1021/nl020208d.

[34] A.J. Waddon, E.B. Coughlin, Crystal structure of polyhedral oligomeric silsequioxane (POSS) nano-materials: a study by X-ray diffraction and electron microscopy, Chem. Mater. 15 (2003) 4555–4561, doi:10.1021/cm034308b.

[35] K. Larsson, K. Larsson, The crystal structure of the 1,3-diglyceride of 3-thiadodecanoic acid, Acta Cryst. 16 (1960) 741–746, doi:10.1107/S0365110X63001948.

[36] A.J. Barry, W.H. Daudt, J.J. Domicone, J.W Gilkey, Crystalline organosilsesquioxanes, J. Am. Chem. Soc. 77 (1955) 4248–4252, doi:10.1021/ja01621a025.

[37] P.T. Mather, H.G. Jeon, A. Romo-Uribe, T.S. Haddad, J.D. Lichtenhan, Mechanical relaxation and microstructure of poly(norbornyl-POSS) copolymers, Macromolecules 32 (1999) 1194–1203, doi:10.1021/ma981210n.

[38] D.M. Smilgies, Scherrer grain-size analysis adapted to grazing-incidence scattering with area detectors, J. Appl. Crystallogr. 42 (2009) 1030–1034, doi:10.1107/S0021889809040126.

[39] X. Li, W.S. Loo, X. Jiang, X. Wang, M.D. Galluzzo, K.I. Mongcopa, A.A. Wang, N.P. Balsara, B.A. Garetz, Confined versus unconfined crystallization in block copolymer/salt mixtures studied by depolarized light scattering, Macromolecules 52 (2019) 982–991, doi:10.1021/acs.macromol.8b02142.

[40] Thelen J.L., Wang A.A., Chen X.C., Jiang X., Schaible E., Balsara N.P. Correlations between salt-induced crystallization, morphology, segmental dynamics, and conductivity in amorphous block copolymer electrolytes. *Macromolecules* (2018) 51:1733–1740. doi:10.1021/acs.macromol.7b02415

[41] K. Pielichowski, K. Flejtuch, Differential scanning calorimetry studies on poly(ethylene glycol) with different molecular weights for thermal energy storage materials, Polym. Adv. Technol. 13 (2002) 690–696, doi:10.1002/pat.276.

[42] A.M. Mayes, La Olvera De, M. Cruz, Microphase separation in multiblock copolymer melts, J. Chem. Phys. 91 (1989) 7228–7235, doi:10.1063/1.457290.

[43] O. Borodin, G.D. Smith, Mechanism of ion transport in amorphous poly(ethylene oxide)/LiTFSI from molecular dynamics simulations, Macromolecules 39 (2006) 1620–1629, doi:10.1021/ma052277v.

[44] K.J. Hou, W.S. Loo, N.P. Balsara, J. Qin, Comparing experimental phase behavior of ion-doped block copolymers with theoretical predictions based on selective ion solvation, Macromolecules 53 (2020) 3956–3966, doi:10.1021/acs.macromol.0c00559.

[45] C.E. Sing, J.W. Zwanikken, La Olvera De, M. Cruz, Ion correlation-induced phase separation in polyelectrolyte blends, ACS Macro Lett. 2 (2013) 1042–1046, doi:10.1021/mz400511r.

[46] I. Nakamura, Z.G. Wang, Thermodynamics of salt-doped block copolymers, ACS Macro Lett. 3 (2014) 708–711, doi:10.1021/mz500301z.

[47] K.J. Hou, J. Qin, Solvation and entropic regimes in ion-containing block copolymers, Macromolecules 51 (2018) 7463–7475, doi:10.1021/acs.macromol.8b01616.

[48] Z. Mester, N.A. Lynd, G.H. Fredrickson, Numerical self-consistent field theory of multicomponent polymer blends in the Gibbs ensemble, Soft Matter. 9 (2013) 11288–11294, doi:10.1039/c3sm51893k.

[49] I. Nakamura, Z.-.G. Wang, Salt-doped block copolymers: ion distribution, domain spacing and effective χ parameter, Soft Matter. 8 (2012) 9356, doi:10.1039/c2sm25606a.

[50] T.H. Epps, T.S. Bailey, H.D. Pham, F.S. Bates, Phase behavior of lithium perchlorate-doped poly (styrene-b-isoprene-b-ethylene oxide) triblock copolymers, Chem. Mater. 14 (2002) 1706–1714, doi:10.1021/cm010971t.

[51] W.S. Loo, X. Jiang, J.A. Maslyn, H.J. Oh, C. Zhu, K.H. Downing, N.P. Balsara, Reentrant phase behavior and coexistence in asymmetric block copolymer electrolytes, Soft Matter. 14 (2018) 2789–2795, doi:10.1039/C8SM00175H.

[52] E.W. Cochran, C.J. Garcia-Cervera, G.H. Fredrickson, Stability of the gyroid phase in diblock copolymers at strong segregation, Macromolecules 39 (2006) 2449–2451, doi:10.1021/ma0527707.

[53] J.D. Vavasour, M.D. Whitmore, Self-consistent field theory of block copolymers with conformational asymmetry, Macromolecules 26 (1993) 7070–7075, doi:10.1021/ma00077a054.